

Artifacts in $T1\rho$ -weighted imaging: Compensation for B_1 and B_0 field imperfections [☆]

Walter R.T. Witschey II ^{a,*}, Arijitt Borthakur ^{a,b}, Mark A. Elliott ^{a,b}, Eric Mellon ^{a,b},
Sampreet Niyogi ^{b,c}, Daniel J. Wallman ^b, Chenyang Wang ^{b,c}, Ravinder Reddy ^{a,b}

^a Graduate Group in Biochemistry & Molecular Biophysics and MMRRCC, University of Pennsylvania, B1 Stellar-Chance Laboratories,
422 Curie Boulevard, Philadelphia, PA 19104-6100, USA

^b Department of Radiology, University of Pennsylvania, Philadelphia, PA, USA

^c Department of Bioengineering, University of Pennsylvania, Philadelphia, PA, USA

Received 4 October 2006; revised 23 January 2007

Available online 26 January 2007

Abstract

The origin of spin locking image artifacts in the presence of B_0 and B_1 magnetic field imperfections is shown theoretically using the Bloch equations and experimentally at low ($\omega_1 \ll \Delta\omega_0$), intermediate ($\omega_1 \sim \Delta\omega_0$) and high ($\omega_1 \gg \Delta\omega_0$) spin locking field strengths. At low spin locking fields, the magnetization is shown to oscillate about an effective field in the rotating frame causing signature banding artifacts in the image. At high spin lock fields, the effect of the resonance offset $\Delta\omega_0$ is quenched, but imperfections in the flip angle cause oscillations about the ω_1 field. A new pulse sequence is presented that consists of an integrated spin echo and spin lock experiment followed by magnetization storage along the $-z$ -axis. It is shown that this sequence almost entirely eliminates banding artifacts from both types of field inhomogeneities at all spin locking field strengths. The sequence was used to obtain artifact free images of agarose in inhomogeneous B_0 and B_1 fields, off-resonance spins in fat and *in vivo* human brain images at 3 T. The new pulse sequence can be used to probe very low frequency (0–400 Hz) dynamic and static interactions in tissues without contaminating B_0 and B_1 field artifacts.

© 2007 Elsevier Inc. All rights reserved.

Keywords: Spin locking; $T1\rho$; Relaxation; Off-resonance $T1\rho$; Inhomogeneous B_0 and B_1 fields

1. Introduction

Magnetic resonance (MR) tissue contrast depends on differences in tissue relaxation times $T1$ and $T2$, diffusion-weighting, magnetization transfer (MT) or perfusion effects to distinguish healthy and diseased tissues. In addition to these conventional contrast techniques, a powerful method to create tissue contrast is the spin–lattice relaxation time in the rotating frame ($T1\rho$) characterized first in spectroscopic experiments by Redfield [1].

$T1\rho$ -weighted contrast is obtained by allowing magnetization to relax under the influence of an on-resonance, continuous wave (cw) radiofrequency (RF) pulse. $T1\rho$ -weighted contrast is sensitive to both low frequency motional processes and static processes. Low frequency motional processes in tissues include proton exchange with hydroxyl or amide groups in proteins [2–4] while static processes include static dipolar interactions [5]. In particular, $T1\rho$ -weighted contrast has distinguished early acute cerebral ischemia in rats [6–8], human gliomas [9] and tumor in breast tissues [10], tracked the early degeneration of cartilage in osteoarthritis [11] and the nucleus pulposus of lumbar intervertebral discs [12] and indirectly detected metabolic $H_2^{17}O$ *in vivo* [13–16].

Variations of the preparatory pulse cluster used for $T1\rho$ -weighted imaging are listed in Table 1. Two popular implementations involve either a rotary echo [17,18] or

[☆] This study was performed at the Metabolic Magnetic Resonance Research and Computing Center, an NIH-supported resource center (NIH RR02305) supported by Grants R01AR045404 and R01AR051041.

* Corresponding author. Fax: +1 215 573 2113.

E-mail address: witschey@med.upenn.edu (W.R.T. Witschey II).

Table 1
Sources of artifacts in $T1\rho$ -weighted imaging and their pulse sequence correction schemes

Spin lock sequence	Reference	B_1 insensitivity	Flip angle ($\alpha = 90^\circ$)	ΔB_0 insensitivity	Off-resonance
<i>Conventional</i>					
Adiabatic ($\omega_{1\max} \gg \Delta\omega_0$)	[8]	X			
Rotary echo (B_1 insensitivity)	[17]	X	X		
Off-resonance	[21,22]	X	X		X
ΔB_0 insensitivity	[25]	X		X	
B_1 and ΔB_0 insensitivity	This manuscript	X	X	X	

$T1\rho$ clusters with adiabatic excitation and storage pulses are complementary to the four pulse sequences analyzed in this paper.

adiabatic excitation [10] to compensate for B_1 inhomogeneities. A degree of ΔB_0 insensitivity is achieved using offset-independent adiabatic pulses, particularly those of the HS*n* family, however, there are restrictions on the minimum $\omega_{1\max}$ needed for a uniform flip angle across the sample [19]. Variations of the spin lock may also be used for low SAR acquisition by manipulating the $T1\rho$ -weighting in k -space [20] or by spin-locking off-resonance [21,22]. In addition, the spin locking pulse may be substituted with an adiabatic full passage pulse train to modulate $T1\rho$ -weighted contrast dynamically during the preparation period [23].

Ideally, to achieve maximum $T1\rho$ -weighted contrast, the spin locking amplitude ($\omega_1 = \gamma B_1$) should coincide with the $T1\rho$ dispersion corresponding to the physical process involved, although, in practice, possible spin lock amplitudes are compromised by B_0 field gradient artifacts and the high specific absorption rate (SAR) of radiation delivered to tissues. Rotary echoes or adiabatic excitation combined with a high amplitude spin lock ($\omega_1 \gg \Delta\omega_0$) remove artifacts from gradients in the B_1 and B_0 field [24], however, increasing ω_1 to reduce artifacts and decreasing ω_1 to reduce SAR is a vice, limiting the acceptable spin lock amplitude on 1.5 and 3 T clinical scanners to $\omega_1 = 400$ – 600 Hz to obtain a $T1\rho$ -weighted image. Also, as scanners continue to increase in field strength to 7 T, there may be no range over which ω_1 is acceptable. A technique to widen the acceptable spin lock range is necessary, particularly in the low-frequency regime where useful clinical contrast is generated by the scalar coupling between ^1H and ^{17}O in studies of brain metabolism or static dipole–dipole or ^1H exchange dynamics in human cartilage.

Here, we examine the origin of ΔB_0 and B_1 spin locking artifacts using the Bloch equations and analyze a new pulse sequence which significantly corrects for these artifacts. This sequence allows spin lock amplitudes in the $\omega_1 = 0$ – 600 Hz range and is demonstrated on an agarose phantom, a water and fat phantom and *in vivo* in the human brain.

2. Theory

2.1. General spin lock

A general pulse sequence for spin locking is shown in Fig. 1. In the following sections, we will analyze how the choice of phase or pulse composition in the above sequence

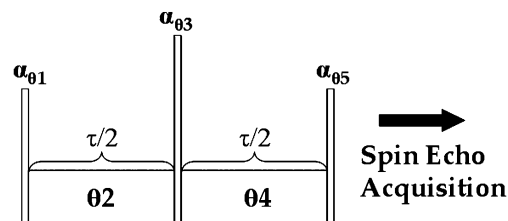


Fig. 1. A generalized pulse sequence for $T1\rho$ -weighted imaging. Each pulse is characterized by a flip angle α and phase θ . Spin locking pulses have both an amplitude ω_1 and phase θ . Each of the four fixed amplitude spin lock pulse sequences in Sections 2.2–2.5 are special cases of this generalized sequence.

can be used to eliminate artifacts from variations in the B_0 or B_1 fields.

Using the Bloch equations, we can trace the path of the magnetization vector $\mathbf{M}(\mathbf{r}; t) = [M_x(\mathbf{r}; t), M_y(\mathbf{r}; t), M_z(\mathbf{r}; t)]^T$ at the spatial location $\mathbf{r} = [\mathbf{x}, \mathbf{y}, \mathbf{z}]$ and time t during the conventional spin locking pulse sequence (Fig. 1). Prior to excitation, the magnetization vector in the rotating frame is

$$\mathbf{M}(\mathbf{r}; 0^-) = [0, 0, M_0(\mathbf{r}; 0^-)]^T \quad (1)$$

where M_0 denotes the equilibrium magnetization and $t = 0^-$ is the time prior to excitation and T denotes the transpose operation. An instantaneous RF pulse may be represented compactly in matrix notation by terms like $R_\theta(\alpha)$, where R denotes a matrix rotation, θ the pulse phase and α the pulse flip angle. Ideally, magnetization is excited by an instantaneous $R_{\theta_1}(90^\circ)$ (phase = θ_1) pulse in the conventional spin locking sequence, however, variations in the B_1 field may cause imperfect 90° flip angles across the sample, such that the flip angle α is instead

$$\alpha(\mathbf{r}) = \gamma \mathbf{B}_1(\mathbf{r}) \tau \quad (2)$$

where B_1 is the actual RF field strength. While an ideal B_1 field is uniform across the sample, e.g. $\mathbf{B}_1(\mathbf{r}) = \mathbf{B}_1$, the field may vary significantly in commercial systems with volume head coils.

After excitation, the magnetization is

$$\mathbf{M}(0^+) = \mathbf{R}_{\theta_1}(\alpha) \mathbf{M}(0^-) \quad (3)$$

where the spatial coordinate \mathbf{r} is dropped for simplicity. Magnetization is now spin locked by a long duration RF pulse for a time τ . Ideally, nuclear spins are on-resonance

during the spin lock, but B_0 field gradients give a distribution of spins about resonance. Off-resonance magnetization is incorporated into the Bloch equations, neglecting relaxation

$$\frac{d\mathbf{M}(t)}{dt} = \gamma\mathbf{M}(t) \times \mathbf{B}(t) \quad (4)$$

where the effective magnetic field in the rotating frame is

$$\mathbf{B}(t) = \left[B_1 \cos \theta_2, B_1 \sin \theta_2, B_0 - \frac{\omega}{\gamma} \right]^T \quad (5)$$

Here, ω is frequency of the rotating frame coordinate system chosen to coincide with the RF pulse carrier frequency ω_{RF} , $\omega_0 = \gamma B_0$ is the spin Larmor frequency, θ_2 is the phase of the spin locking pulse and we assume $\omega_1 \ll \omega_0$. Of course, on-resonance $\omega_{\text{RF}} = \omega_0$, but we relax this assumption in Eq. (5) because of inhomogeneity in the B_0 field. The solutions to Eq. (4) cause the net magnetization to nutate about the axis of the effective field z' , which makes an angle with the z -axis

$$\varphi = \tan^{-1} \left(\frac{\omega_1}{\Delta\omega_0} \right) \quad (6)$$

where $\Delta\omega_0 = \omega_0 - \omega_{\text{RF}}$. In matrix notation $\mathbf{M}(t + \tau) = \mathbf{R}_{z'}(\omega_{\text{eff}}\tau)\mathbf{M}(t)$, magnetization evolves during the spin locking pulse under the influence of the effective field

$$|\omega_{\text{eff}}| = \sqrt{\omega_1^2 + \Delta\omega_0^2} \quad (7)$$

by the off-resonance pulse propagator $\mathbf{R}_{z'}(\omega_{\text{eff}}\tau)$. The nutation of the magnetization vector around the effective field is described by transformation to the tilted rotating frame

$$\mathbf{R}_{z'}(\omega_{\text{eff}}\tau) = \mathbf{R}_{\theta_2}(\varphi)\mathbf{R}_z(\omega_{\text{eff}}\tau)\mathbf{R}_{\theta_2}(-\varphi) \quad (8)$$

Magnetization is now flipped by another instantaneous pulse $\mathbf{R}_{\theta_3}(\alpha_2)$ after which it is spin locked by another cw pulse with phase θ_4 and instantaneously flipped one last time. The final magnetization after this series of rotations and spin locks is

$$\mathbf{M}(\tau^+) = \mathbf{R}_{\theta_3}(\alpha_3)\mathbf{R}_{\theta_4}(\varphi)\mathbf{R}_z(\omega_{\text{eff}}\tau/2)\mathbf{R}_{\theta_4}(-\varphi)\mathbf{R}_{\theta_3}(\alpha_2) \mathbf{R}_{\theta_2}(\varphi)\mathbf{R}_z(\omega_{\text{eff}}\tau/2)\mathbf{R}_{\theta_2}(-\varphi)\mathbf{R}_{\theta_1}(\alpha_1)\mathbf{M}(0^-) \quad (9)$$

It is possible to further generalize Eq. (9) by making the first and second cw durations and amplitudes inequivalent, however, we will instead simplify to examine special cases of Eq. (9).

2.2. Conventional spin lock: $90_{x-\tau}y-90_{-x}$

The conventional spin lock pulse cluster is sensitive to variations in both the B_0 and B_1 magnetic fields. While the conventional spin lock is in regular use in spectroscopy, it is replaced by adiabatic and rotary echo methods at spin lock amplitudes $\omega_1 \gg \Delta\omega_0$ in MR imaging.

For conventional spin locking, Eq. (9) reduces to

$$\mathbf{M}(\tau^+) = \mathbf{R}_{-x}(\alpha)\mathbf{R}_y(\varphi)\mathbf{R}_z(\omega_{\text{eff}}\tau/2)\mathbf{R}_y(-\varphi)\mathbf{R}_x(\alpha)\mathbf{M}(0^-) \quad (10)$$

After excitation, the magnetization is

$$\mathbf{M}(0^-) = \begin{bmatrix} 0 \\ M_0 \sin \alpha \\ M_0 \cos \alpha \end{bmatrix} \quad (11)$$

After the full spin locking duration τ , the magnetization is

$$\mathbf{M}(\tau^-) = \begin{bmatrix} 1 & & & \\ & \cos(\varphi) & \sin(\varphi) & \\ & -\sin(\varphi) & \cos(\varphi) & \\ & & & 1 \end{bmatrix} \begin{bmatrix} \cos(\omega_{\text{eff}}\tau) & \sin(\omega_{\text{eff}}\tau) \\ -\sin(\omega_{\text{eff}}\tau) & \cos(\omega_{\text{eff}}\tau) \end{bmatrix} \begin{bmatrix} 0 \\ M_0 \sin \alpha \\ M_0 \cos \alpha \end{bmatrix} \quad (12)$$

Finally, the $T1\rho$ -weighted magnetization is stored longitudinally with a final α_{-x} pulse, where, including inhomogeneity in the RF field

$$\mathbf{M}(\tau^+) = \begin{bmatrix} \mathbf{M}_x(\tau^-) \\ -\mathbf{M}_y(\tau^-) \sin \alpha \\ \mathbf{M}_z(\tau^-) \cos \alpha \end{bmatrix} \quad (13)$$

A spoiler gradient eliminates the residual transverse magnetization, so the final longitudinal magnetization

$$\mathbf{M}_z(\tau^+) = M_0 [\cos(\omega_{\text{eff}}\tau) \sin(-\alpha + \varphi) \sin(\alpha + \varphi) + \cos(-\alpha + \varphi) \cos(\alpha + \varphi)] \quad (14)$$

where α , ω_{eff} and φ are functions of \mathbf{r} . If the B_1 field strength is much greater than the resonance offset ($\omega_1 \gg \Delta\omega$), then the angle φ between z'' and z is nearly 90° . This amounts to a 90° phase shift of angular terms in Eq. (14), so

$$(\omega_1 \gg \Delta\omega_0) \quad \mathbf{M}_z(\mathbf{r}; \tau^+) = M_0 [\cos(\omega_1\tau) \cos^2(\alpha) - \sin^2(\alpha)] \quad (15)$$

When α is not 90° , there is a cosinusoidal $\omega_1\tau$ dependence to the magnetization. These artifacts appear as oscillating regions of signal intensity arranged along the gradients of the B_1 field. We show this special case in Fig. 2a.

Conversely, if $\omega_1 \ll \Delta\omega_0$, then the angle φ between z'' and z is nearly 0° and

$$(\omega_1 \ll \Delta\omega_0) \quad \mathbf{M}_z(\mathbf{r}; \tau^+) = M_0 [-\cos(\Delta\omega\tau) \sin^2(\alpha) + \cos^2(\alpha)] \quad (16)$$

When α is 90° , $T1\rho$ -weighted images are contaminated with artifacts due to gradients in the B_0 field because of the first term in Eq. (16).

2.3. B_1 insensitive spin lock: $90_{x-\tau}2y-\tau/2_{-y}90_{-x}$

The B_1 insensitive spin lock applies Solomon's rotary echo to imaging pulse sequences [24]. Charagundla et al. implemented the rotary echo to remove the signal dependence of the variation in the B_1 field [17]. Instead of a single, long duration spin lock, the pulse is separated into two equal duration pulses with opposite phase $\pm y$ and Eq. (9) is reduced to

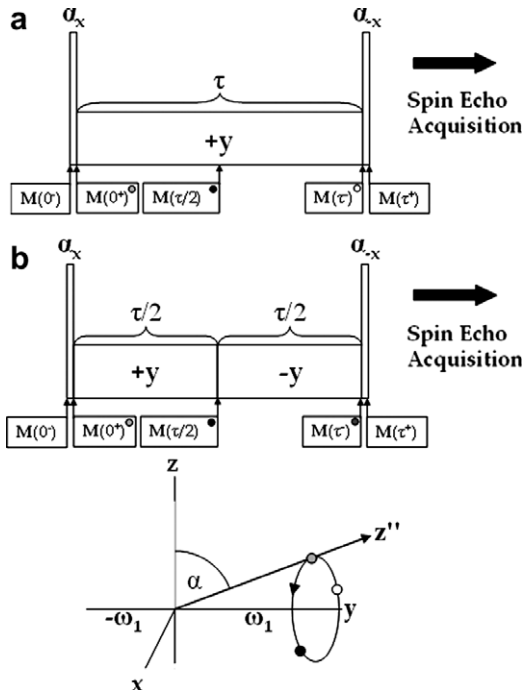


Fig. 2. Conventional (a) and rotary echo (b) composite pulses for $T1\rho$ relaxation measurements and the magnetization path during on-resonance spin locking pulse. Magnetization flipped at an angle α with the y -axis (grey) nutates about the ω_1 or y -axis and at $\tau/2$ accumulates a phase $\omega_{\text{eff}}\tau/2$ (black). While the traditional pulse sequence continues accumulating phase in the same direction (white), the rotary echo returns the magnetization back to its initial position (grey).

$$\mathbf{M}(\tau^+) = \mathbf{R}_{-x}(\alpha)\mathbf{R}_x(\varphi)\mathbf{R}_z(\omega_{\text{eff}}\tau/2)\mathbf{R}_x(-\varphi)\mathbf{R}_x(\varphi) \times \mathbf{R}_z(\omega_{\text{eff}}\tau/2)\mathbf{R}_x(-\varphi)\mathbf{R}_x(\alpha)\mathbf{M}(0^-) \quad (17)$$

During the second $\tau/2$ spin locking pulse, the effective field angle

$$-\varphi = \tan^{-1}\left(\frac{-\omega_1}{\Delta\omega}\right) \quad (18)$$

is rotated in the opposite sense about the z -axis.

The full expression for the longitudinal magnetization is extensive and is more easily implemented in matrix form as Eq. (17), however, in the limit $\omega_1 \gg \Delta\omega_0$, $\varphi = 90^\circ$ and Eq. (17) becomes

$$(\omega_1 \gg \Delta\omega_0) \quad \mathbf{M}(\tau^+) = \mathbf{R}_{-x}(\alpha)\mathbf{R}_{-y}(\omega_{\text{eff}}\tau/2)\mathbf{R}_y(\omega_{\text{eff}}\tau/2)\mathbf{R}_x(\alpha)\mathbf{M}(0^-) \quad (19)$$

Which, because $\mathbf{R}_{-y}\mathbf{R}_y = 1$ and $\mathbf{R}_x(\alpha)\mathbf{R}_x(-\alpha) = 1$, may be simplified to

$$(\omega_1 \gg \Delta\omega_0) \quad \mathbf{M}(\tau^+) = \mathbf{M}(0^-) \quad (20)$$

where the direction of the effective field is entirely along $+y$ for the first τ period and along $-y$ for the second. The signal at $M(\tau^+)$ no longer depends on $\cos(\omega_1\tau)$ or α and so the image is free of banding artifacts inherent to the conventional spin lock. The B_1 insensitive pulse cluster is ideal for situations where the B_1 field greatly exceeds the resonance offset (see Fig. 2b).

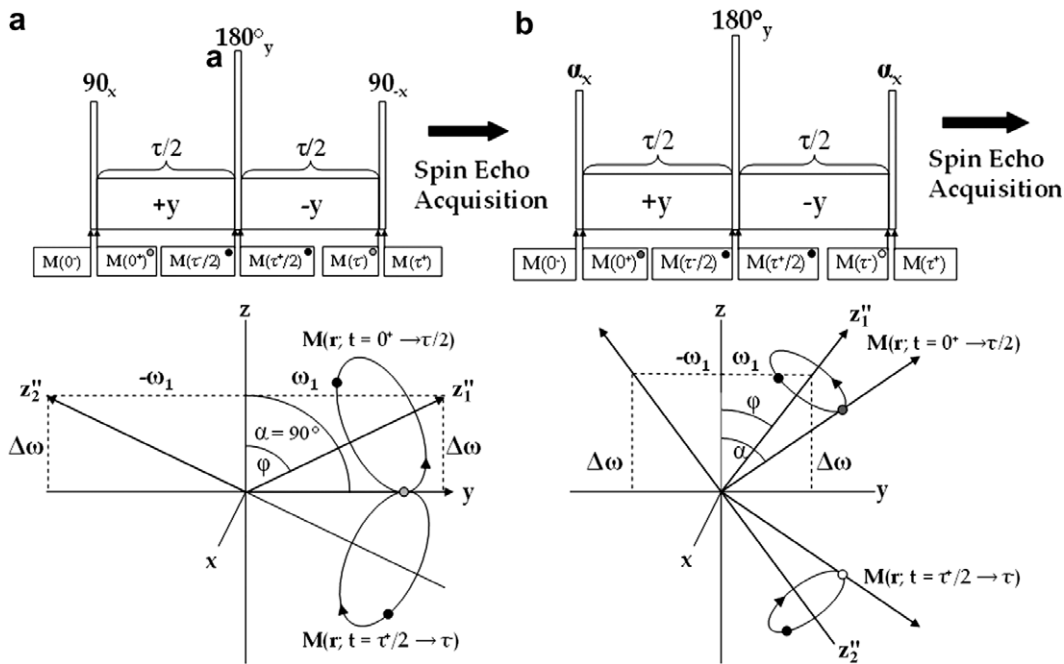


Fig. 3. ΔB_0 insensitive (a) and B_1 and ΔB_0 insensitive (b) composite pulses for $T1\rho$ weighted imaging and the magnetization path during each sequence. In (a) magnetization is flipped along the y -axis (grey), where it nutates about the effective field (z' -axis) and at time $\tau/2$ (black) is flipped 180° about the y -axis where it nutates around the effective field (z'' -axis) back along the y -axis (grey). In (b) the magnetization follows a similar path, but with two differences: (1) the excitation flip angle does not need to be 90° and (2) B_1 insensitivity is maintained by flipping the magnetization along the $-z$ -axis. While (b) is more robust than (a), an imperfect 180° flip can still produce artifacts.

On the other hand, if $\omega_1 \ll \Delta\omega_0$, Eq. (17) may be reduced to

$$\mathbf{M}(\tau^+) = \mathbf{R}_x(\alpha)\mathbf{R}_z(\Delta\omega\tau)\mathbf{R}_x(-\alpha)\mathbf{M}(0^-) \quad (21)$$

and the $T1\rho$ -weighted longitudinal component is the same as the conventional spin lock (Eq. (16)).

2.4. ΔB_0 insensitive spin lock: $90_{x-\tau/2}y-180_{y-\tau/2}y-90_{-x}$

Avison et al. introduced a spin locking pulse cluster which compensates for gradients in the B_0 field, but does not eliminate artifacts from imperfect flip angles $\alpha = 90^\circ$ (Fig. 3a) [25]. With a 2α (ideally, $2\alpha = 180^\circ$) pulse between the spin locking pulse clusters Eq. (9) reduces to

$$\mathbf{M}(\tau^+) = \mathbf{R}_x(\alpha)\mathbf{R}_x(\varphi)\mathbf{R}_z''(\omega_{\text{eff}}\tau/2)\mathbf{R}_x(-\varphi)\mathbf{R}_y(2\alpha)\mathbf{R}_x(-\varphi) \quad (22)$$

$$\mathbf{R}_z''(\omega_{\text{eff}}\tau/2)\mathbf{R}_x(\varphi)\mathbf{R}_x(-\alpha)\mathbf{M}(0^-)$$

If $\omega_1 \gg \Delta\omega_0$, $\varphi = 90^\circ$, and Eq. (22) becomes

$$(\omega_1 \gg \omega_0) \quad \mathbf{M}(\tau^+) = \mathbf{R}_{-x}(\alpha)\mathbf{R}_{-y}(\omega_1\tau/2)\mathbf{R}_y(2\alpha)\mathbf{R}_y(\omega_1\tau/2) \quad (23)$$

$$\times \mathbf{R}_x(\alpha)\mathbf{M}(0^-)$$

If the initial flip angle $\alpha = 90^\circ$, then the magnetization is entirely along $+y$ during both spin lock periods, $\mathbf{R}_y(2\alpha)$ has no effect on the magnetization directed along $+y$ and the result is Eq. (20). Allowing for B_1 imperfections, $\alpha = 90^\circ$ and the final longitudinal magnetization

$$(\omega_1 \gg \Delta\omega_0) \quad \mathbf{M}_z(\tau^+) = \mathbf{M}_0[\sin^2(\alpha) + \cos^2(\alpha)\cos(2\alpha)] \quad (24)$$

does not depend on the nutation frequency $\cos(\omega_1\tau)$. Conversely, if $\omega_1 \ll \Delta\omega_0$, then $\varphi = 0^\circ$ and we rewrite Eq. (23) as

$$(\omega_1 \ll \Delta\omega_0) \quad \mathbf{M}(\tau^+) = \mathbf{R}_{-x}(\alpha)\mathbf{R}_z(\Delta\omega_0\tau/2)\mathbf{R}_y(2\alpha) \quad (25)$$

$$\times \mathbf{R}_z(\Delta\omega_0\tau/2)\mathbf{R}_x(\alpha)\mathbf{M}(0^-)$$

Specifically, if $\mathbf{R}_y(2\alpha) = \mathbf{R}_y(180^\circ)$, then Eq. (25) reduces to Eq. (20) and is independent of off-resonance effects $\Delta\omega_0$. At intermediate field strengths ($\omega_1 \sim \Delta\omega_0$), however, Eq. (22) requires both $\mathbf{R}_x(\alpha) = \mathbf{R}_x(90^\circ)$ and $\mathbf{R}_y(2\alpha) = \mathbf{R}_y(180^\circ)$ to remove terms like $\cos(\omega_{\text{eff}}\tau)$ and this requirement is almost never satisfied across the sample.

2.5. ΔB_0 and B_1 insensitive spin lock: $90_{x-\tau/2}y-180_{y-\tau/2}y-90_x$

Alternating the phase of the last 90° pulse in the spin lock pulse cluster aligns the final magnetization along the $-z$ -axis rather than along the $+z$ -axis (Fig. 3b). The alternation of the phase of the final 90° pulse from $-x$ to $+x$ in the cluster compensates for imperfect flip angles $\alpha = 90^\circ$ in an inhomogeneous B_1 field. The expression for the full pulse propagator is the same as Eq. (22) except for the final phase shift

$$\mathbf{M}(\tau^+) = \mathbf{R}_x(-\alpha)\mathbf{R}_x(\varphi)\mathbf{R}_z''(\omega_{\text{eff}}\tau/2)\mathbf{R}_x(-\varphi)\mathbf{R}_y(2\alpha) \quad (26)$$

$$\mathbf{R}_x(-\varphi)\mathbf{R}_z''(\omega_{\text{eff}}\tau/2)\mathbf{R}_x(\varphi)\mathbf{R}_x(-\alpha)\mathbf{M}(0^-)$$

If $\omega_1 \gg \Delta\omega_0$, then $\varphi = 90^\circ$ and Eq. (26) reduces to

$$(\omega_1 \gg \Delta\omega_0) \quad \mathbf{M}(\tau^+) = \mathbf{R}_x(\alpha)\mathbf{R}_{-y}(\omega_1\tau/2)\mathbf{R}_y(2\alpha) \quad (27)$$

$$\times \mathbf{R}_y(\omega_1\tau/2)\mathbf{R}_x(\alpha)\mathbf{M}(0^-)$$

and the final longitudinal magnetization is

$$(\omega_1 \gg \Delta\omega_0) \quad \mathbf{M}_z(\tau^+) = \mathbf{M}_0[-\sin^2(\alpha) + \cos^2(\alpha)\cos(2\alpha)] \quad (28)$$

and is identical to Eq. (24) but with the first term inverted. The implication is that if $\alpha = 90^\circ$, the absolute magnetization is unaffected by the pulse phase shift. Instead, if $\omega_1 \ll \Delta\omega_0$ then magnetization is

$$(\omega_1 \ll \Delta\omega_0) \quad \mathbf{M}(\tau^+) = \mathbf{R}_x(\alpha)\mathbf{R}_z(\Delta\omega_0\tau/2)\mathbf{R}_y(2\alpha) \quad (29)$$

$$\times \mathbf{R}_z(\Delta\omega_0\tau/2)\mathbf{R}_x(\alpha)\mathbf{M}(0^-)$$

The key feature of Eqs. (26) and (29) is that the final phase shift $-x$ to $+x$ no longer requires that $\mathbf{R}_x(\alpha) = \mathbf{R}_x(90^\circ)$, however, to completely reduce Eq. (29) to Eq. (20) we still require $\mathbf{R}_y(2\alpha) = \mathbf{R}_y(180^\circ)$. In this case Eq. (29) becomes

$$(\omega_1 \ll \Delta\omega_0) \quad \mathbf{M}(\tau^+) = -\mathbf{M}(0^-) \quad (30)$$

$$R_y(2\alpha) = R_y(180^\circ),$$

Despite the inability to achieve a perfect 180° flip in practice, artifacts are less severe than in the ΔB_0 insensitive spin lock. In addition, the rectangular 180° may be substituted with a composite 180° RF pulse to further reduce these artifacts [26].

3. Methods

Imaging was performed on a Siemens Trio 3T clinical imaging system equipped with a Bruker birdcage head coil. To maintain consistent B_0 and B_1 field maps throughout the experiment, automated single slice shim and pulse calibration was performed once and without any further adjustments. Volunteers were recruited to the study and scanned following a pre-approved protocol, described below, by the Institutional Review Board of the University of Pennsylvania. Agarose (3% w/v, 200 mM ^{23}Na) or water/fat phantom (150 mL mineral oil/200 mL doped H_2O) imaging was performed using a similar protocol (FOV = 15 cm^2).

A B_0 field map (Figs. 4, 6–8) was obtained from four complex gradient echo images with TE = 5, 10, 15 and 20 ms, TR = 700 ms, FOV = 23 cm^2 , slice thickness = 4 mm and BW = 130 Hz/pixel. Following phase unwrap, the accumulated pixel phase $\Delta\theta_0$ was related to the frequency offset by

$$\Delta\omega_0\Delta\text{TE} = \Delta\theta_0 \quad (31)$$

The final B_0 field map was obtained by minimizing pixel by pixel the chi-square error statistic to Eq. (31) given the image echo times (TE) and pixel phases ($\Delta\theta_0$) using a linear least squares fitting algorithm in IDL (ITT Visual Information Solutions, Boulder, CO).

A B_1 field map (Figs. 4, 6–8) was obtained using the following protocol. Four images were obtained with varied rectangular pulse duration $\tau = 150, 200, 250$ and $300 \mu\text{s}$ using a single rectangular pulse θ_x followed by a spoiler

gradient and 2D single slice fast spin echo frequency and phase encoding sequence with the following imaging parameters: $TE_{\text{eff}}/TR = 13/2500$ ms, 128×128 image matrix, $FOV = 23$ cm², slice thickness = 4 mm, echo train length = 7, $BW = 130$ Hz/pixel. B_1 field maps were generated using a function in IDL based on the Levenberg–Marquardt algorithm [27] to compute a non-linear least squares fit to the function

$$S(\tau) = S(0) \cos(\omega_1 \tau) \quad (32)$$

where $S(\tau)$ denotes pixel signal in an image with rectangular pulse duration τ and ω_1 is the B_1 field amplitude.

Post-processing of both the ΔB_0 and B_1 field maps involved zeroing non-finite pixel values, 3×3 boxcar smoothing filter and a binary mask of linear fits with $R^2 < 0.995$.

Four variations of a pulse cluster used for $T1\rho$ -weighting (described each in Sections 2.2–2.5) were followed by a gradient to spoil residual transverse magnetization and a 2D single slice fast spin echo frequency and phase encoding sequence with spin lock duration ($\tau = \text{TSL}$) = 40 ms, $\omega_1 = 0, 25$ or 400 Hz, echo train length = 7, $BW = 130$ Hz/pixel.

To verify the experimentally acquired $T1\rho$ -weighted images (Figs. 4, 6–8), simulated images were created from experimental ΔB_0 and B_1 field maps using the Bloch equations with identical $T1\rho$ -weighted imaging parameters: spin lock duration ($\tau = \text{TSL}$) = 40 ms, $\omega_1 = 0, 25$ or 400 Hz. Rather than use explicit solutions to the Bloch equations for each pulse sequence Eqs. (14), (17), (22) and (26), it was fortuitous to use the generalized matrix notation of Eq. (9), however, Figs. 4 and 6 do not incorporate artifacts from relaxation processes.

The contribution to image artifacts from tissue relaxation and an imperfect refocusing pulse is examined in Figs. 7 and 8. Relaxation was modeled during the spin locking pulses using the transient solutions to the Bloch equations Eq. (28). In the tilted rotating frame, the matrix formulation for both precession about the effective field and relaxation is

$$R_{z''}(\omega_{\text{eff}}\tau) = \begin{bmatrix} \cos(\omega_{\text{eff}}\tau)e^{-\tau/T2\rho} & \sin(\omega_{\text{eff}}\tau)e^{-\tau/T2\rho} \\ -\sin(\omega_{\text{eff}}\tau)e^{-\tau/T2\rho} & \cos(\omega_{\text{eff}}\tau)e^{-\tau/T2\rho} \end{bmatrix} e^{-\tau/T1\rho} \quad (33)$$

In general, both $T1\rho$ and $T2\rho$ are dependent on the B_0 and B_1 fields and may be written as $T1\rho(\Delta\omega_0 = 0, \omega_1)$ and $T2\rho(\Delta\omega_0 = 0, \omega_1)$ or, for arbitrary $\Delta\omega_0$, $T1\rho_{\text{off}}(\Delta\omega_0, \omega_1)$ and $T2\rho_{\text{off}}(\Delta\omega_0, \omega_1)$. In addition, the steady-state solution to the Bloch equations requires an additional term

$$\mathbf{M}(\tau^+) = \mathbf{R}_z(\omega_{\text{eff}}\tau)\mathbf{M}(\tau^-) + M_{\text{ss}}(1 - e^{-\tau/T1\rho})\mathbf{z}'' \quad (34)$$

where \mathbf{z}'' denotes the unit vector in the direction of the effective field and M_{ss} is the steady-state magnetization. The rotary echo further complicates an analysis of relaxa-

tion, since the magnetization approaches two distinct steady-states during each period.

Relaxation-dependent artifacts were examined by substituting Eq. (33) and (34) into Eq. (8) with $T1\rho$ and $T2\rho$ as unknowns. The steady-state magnetization was fixed ($M_{\text{ss}} = 0$) for the simulation. $T1\rho$ and $T2\rho$ relaxation maps were calculated from Eq. (9) using a Levenberg–Marquardt algorithm Eq. (27) in IDL using initial estimates $T1\rho = 50$ ms and $T2\rho = 140$ ms.

The specific absorption rate (SAR) delivered during the $T1\rho$ -weighted sequences was determined by estimating the SAR during an arbitrary RF pulse [29]:

$$\text{SAR}_{\tau/\alpha} = f \left(\frac{3 \text{ ms}}{\tau} \right)^2 \left(\frac{\alpha}{90^\circ} \right)^2 \text{SAR}_{3\text{ms}/90^\circ} \quad (35)$$

where $\text{SAR}_{3 \text{ ms}/90^\circ}$ is the average SAR delivered to the head during a 3 ms rectangular pulse with flip angle $\alpha = 90^\circ$ using a quadrature birdcage coil, f is the pulse shape factor (rectangular pulse = 1.0, sinc pulse = 2.0), τ is the RF pulse duration and α is the RF pulse flip angle. For example, the average $\text{SAR}_{3 \text{ ms}/90^\circ}$ in the brain (W/kg) at 3 T for a quadrature birdcage coil is between 0.242 W/kg (1.5 T) and 2.16 W/kg (4.1 T). For a generalized pulse sequence, the average SAR delivered is the sum of the energy absorbed by each RF pulse divided by the total time to acquire the image

$$\text{SAR} = \frac{\sum_{n=1}^N \text{SAR}_{\tau_n/\alpha_n} \tau_n}{\text{TT}} \quad (36)$$

where SAR denotes the average delivered SAR over a total time period TT and τ_n is the n th RF pulse duration and α_n the n th RF pulse flip angle. The FDA limits the delivered SAR to 3 W/kg averaged over the head during a 10 min period and assuming continuous scanning during this period, 3 W/kg per TR. Eq. (36) estimates the average SAR delivered to the brain (Fig. 6) during the $T1\rho$ -weighted sequences is approximately 0.5 W/kg/TR at $\omega_1 = 400$ Hz and 0.08 W/kg/TR at $\omega_1 = 25$ Hz. By comparison, the SAR delivered during a $T1\rho$ -weighted sequence with $\text{TSL} = 100$ ms at $\omega_1 = 800$ Hz is 3.8 W/kg/TR, surpassing FDA regulations. The actual SAR may differ from this estimate because of coil and head geometry.

4. Results

We confirmed the theory in 3% agarose phantoms to demonstrate the effectiveness of the four different $T1\rho$ pulse clusters to ΔB_0 and B_1 field gradients. While none of the four pulse clusters completely eliminated artifacts at all spin locking field strengths ($\omega_1 = 0, 25$ and 400 Hz), we found the ΔB_0 and B_1 insensitive pulse cluster was the most robust. The remaining artifacts are attributed to an imperfect 180° pulses, but may be removed using either composite 180° or an adiabatic refocusing pulse.

$T1\rho$ -weighted images were simulated from B_1 and ΔB_0 maps to verify that spin locking artifacts could be modeled

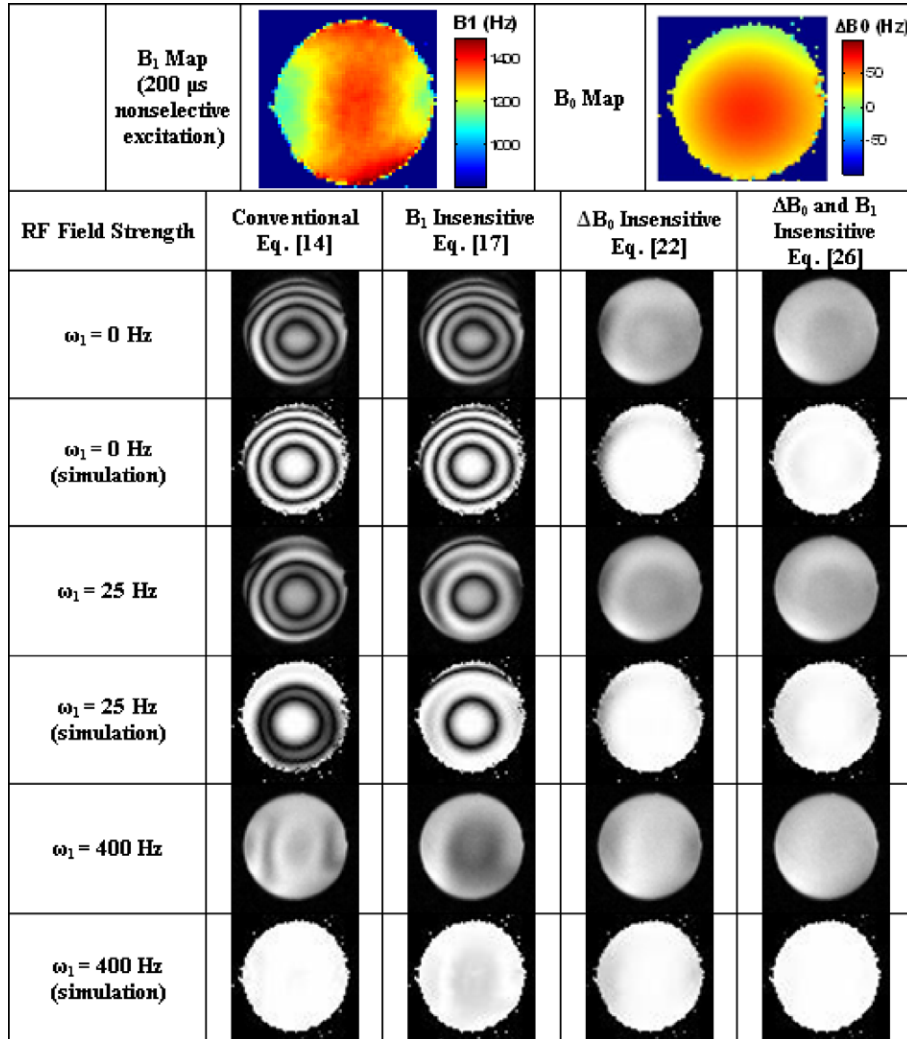


Fig. 4. Simulated and actual spin lock artifacts at TSL = 30 ms in three different ω_1 regimes: (1) $\Delta\omega \gg \omega_1$ ($\omega_1 = 0$ Hz) (2) $\Delta\omega \sim \omega_1$ ($\omega_1 = 25$ Hz) and (3) $\Delta\omega \ll \omega_1$ ($\omega_1 = 400$ Hz). B_1 and B_0 field maps were obtained after automatic pulse calibration and shimming protocols on a Siemens Trio 3T clinical imaging system. The B_1 field map was scaled to an ideal $\pi/2$ flip angle with a 200 μ s rectangular pulse ($\omega_1 = 1250$ Hz). The actual ω_1 amplitude varies throughout the sample. To amplify image artifacts, the excitation and storage pulses were 80° instead of the nominal 90°. Color images available online.

using the Bloch equations. The simulated images were obtained using Eqs. (14), (17), (22) and (26) and are displayed alongside the actual $T1\rho$ -weighted images in Fig. 4. Actual images were collected using four spin locking composite pulse clusters and three different spin locking field strengths ω_1 : (1) $\Delta\omega_0 \gg \omega_1$ ($\omega_1 = 0$ Hz) (2) $\Delta\omega_0 \sim \omega_1$ ($\omega_1 = 25$ Hz) and (3) $\Delta\omega_0 \ll \omega_1$ ($\omega_1 = 400$ Hz).

At $\omega_1 = 400$ Hz and $\Delta\omega_0 \ll \omega_1$, conventional spin locking artifacts described by Eq. (15) are arranged along the gradients of the ω_1 field. Banding artifacts form every $\omega_1\tau = 2\pi$ and while the B_1 insensitive spin lock removes these artifacts, they reemerge in the ΔB_0 insensitive sequence. Inverting the phase of the final 90° pulse $+x$ removes these artifacts.

At $\omega_1 = 0$ Hz and $\Delta\omega \gg \omega_1$, B_0 field gradients create banding artifacts described by Eq. (16). These artifacts are best known among fatty tissues or nasal cavities where the corresponding chemical shift or tissue susceptibility difference gives a large resonance offset. A sample in a Gaussian-like B_0 field gradient forms bands for every $\Delta\omega_0\tau = 2\pi$

and increasing either the resonance offset $\Delta\omega_0$ or the spin lock duration τ increases the total number of bands in the image. The banding artifacts are identical in both the conventional and B_1 insensitive spin locking sequences since, in the limit $\omega_1 \rightarrow 0$, the two sequences are identical. Inserting a 180° pulse theoretically removes the dependence on the resonance offset (from Eq. (25)), but banding artifacts remain from a combination of imperfect 180° (ΔB_0 and B_1 insensitive) and imperfect 90° pulses (ΔB_0 insensitive).

To illustrate full ΔB_0 insensitivity during spin locking, a series of images were collected in a fat and water phantom at varying spin lock durations τ (Fig. 5). At 3 T and $\omega_1 = 500$ Hz, the effective field makes an angle $\varphi \approx 51^\circ$ to the z -axis and produces severe banding artifacts in both conventional and B_1 insensitive $T1\rho$ -weighted imaging. The artifact is removed in ΔB_0 or ΔB_0 and B_1 insensitive pulse clusters provided the hard pulse flip angles (90° or 180°) are conserved.

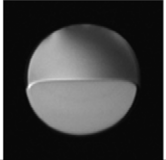
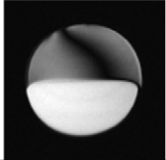
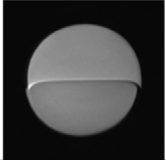
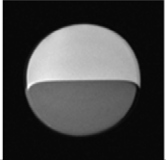
RF Field Strength	Conventional Eq. [14]	B_1 Insensitive Eq. [17]	ΔB_0 Insensitive Eq. [22]	ΔB_0 and B_1 Insensitive Eq. [26]
$\omega_1 = 500$ Hz				

Fig. 5. $T1\rho$ -weighted images of a water (bottom) and fat (top) phantom. Off-resonance fat protons produce artifacts in conventional and B_1 insensitive $T1\rho$ -weighted images, but are absent in ΔB_0 insensitive methods. Contrast between water and fat varies in each of the four pulse sequences and is attributed to the off-resonance relaxation of fat spins.

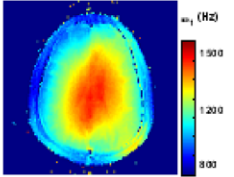
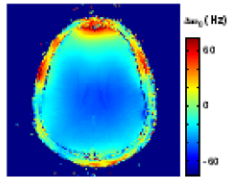
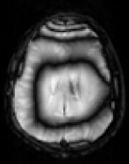
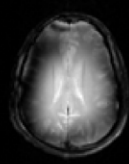
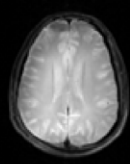
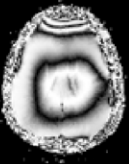


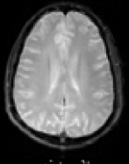
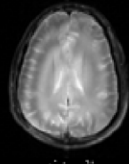
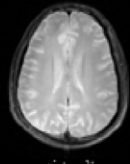



			
RF Field Strength	B_1 Compensation Eq. [17]	B_0 Compensation Eq. [22]	B_1 and B_0 Compensation Eq. [26]
$B_1 = 25$ Hz			
$B_1 = 25$ Hz (simulation)			
$B_1 = 400$ Hz			
$B_1 = 400$ Hz (simulation)			

Fig. 6. $T1\rho$ -weighted images of the brain at 3 T. Low spin lock amplitudes ($\omega_1 = 25$ Hz) induce $\Delta\omega_0$ banding artifacts in both B_1 compensation and B_0 compensation sequence variants. These artifacts are greatly reduced at higher spin lock amplitudes or with both B_1 and B_0 compensation. Color images available online.

$T1\rho$ -weighted images were obtained of the human brain *in vivo* and show significant $\Delta\omega_0$ banding artifacts at low spin lock amplitudes ($\omega_1 \sim \Delta\omega_0$) in Fig. 6. At higher spin lock amplitudes ($\omega_1 \gg \Delta\omega_0$), the magnetization for each of the pulse sequences is described by Eqs. (20), (24) and (28), respectively, and the magnetization is independent of nutation about the effective field. By compensating for both B_1 and B_0 imperfections, artifacts are significantly reduced at $\omega_1 = 25$ Hz as well.

The high artifact suppression in the ΔB_0 and B_1 insensitive pulse sequence shows remarkable robustness to field inhomogeneities despite possible artifacts from relaxation processes. The pulse sequence used for ΔB_0 and B_1 correction, $90_x - \tau/2_y - 180_y - \tau/2_{-y} - 90_x$, is not a unique solution and an alternative such as $90_x - \tau/2_y - 180_{-x} - \tau/2_y - 90_{-x}$ is equally robust (data not shown). Also, there exist two additional solutions for each excitation phase 90_y , 90_{-x} or 90_{-y} .

Additional artifacts emerge because of both tissue relaxation and an imperfect refocusing pulse; these additional

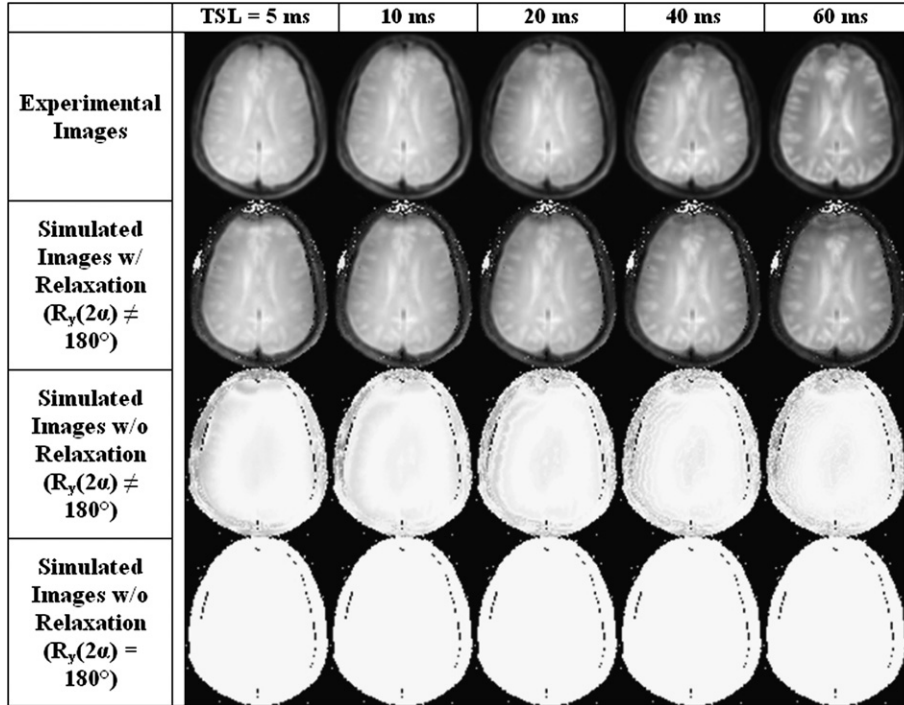


Fig. 7. Experimental and simulated $T1\rho$ -weighted images of the brain using the pulse sequence described in Section 2.5 at a spin locking field strength $\omega_1 = 25$ Hz. Row 1: experimental $T1\rho$ -weighted images obtained for five spin lock durations 5–60 ms. Row 2: simulated $T1\rho$ -weighted images from B_1 and ΔB_0 field maps using transient solutions to the Bloch equations and a parametric fit of the unknown relaxation times $T1\rho$ and $T2\rho$ to the experimental images in Row 1. Row 3: simulated $T1\rho$ -weighted images from B_1 and ΔB_0 field maps to the Bloch equations, neglecting relaxation, but using the actual refocusing pulse $R_y(2\alpha \neq 180^\circ)$. Row 4: simulated $T1\rho$ -weighted images from B_1 and ΔB_0 field maps to the Bloch equations, neglecting relaxation and assuming a perfect refocusing pulse $R_y(2\alpha = 180^\circ)$. Without modeling relaxation, there is consequently no relaxation-dependent contrast in Rows 3 and 4. Artifacts from relaxation effects are predominantly localized to the frontal cortex, suggesting relaxation artifacts are primarily dependent on regions of poor B_0 field homogeneity, such as near nasal cavities. Artifacts from imperfect refocusing pulses localized to the brain periphery where B_1 field inhomogeneity is poor.

artifacts are considered in Fig. 7. Row 1 shows experimental images using the ΔB_0 and B_1 insensitive pulse sequence for five different spin locking durations (TSL = 5, 10, 20, 40, and 60 ms) at $\omega_1 = 25$ Hz. Except for the frontal cortex, a region of significant B_0 field inhomogeneity, the experimental images are free of low ω_1 band artifacts. The location of the artifacts can be reproduced in simulated images that model $T1\rho$ and $T2\rho$ relaxation (Row 2), but are not observed in simulations that do not model relaxation (Row 4). To some extent, an imperfect refocusing pulse produces artifacts around the periphery in regions of significant B_1 field inhomogeneity (Row 3) and also in the frontal cortex.

The relationship between tissue relaxation, field inhomogeneity and the residual artifacts may be considered as follows: as magnetization nutates around the effective field, the component parallel to the effective field M_{\parallel} will decay to the steady-state magnetization at a rate $1/T1\rho$ and the component perpendicular to the effective field M_{\perp} will decay at a rate $1/T2\rho$. As the ratio M_{\perp}/M_{\parallel} changes during the spin lock, so does the nutation angle between the effective field and magnetization. If the nutation angle changes, the final spin locked magnetization (Eq. (30)) will not be stored parallel to the $-z$ -axis and field-dependent artifacts

may emerge. Therefore, field inhomogeneity has two primary effects, to nutate the magnetization different angles because of variations in ω_{eff} and also to cause relaxation-dependent artifacts. As Figs. 6 and 7 demonstrate, small field inhomogeneities have a substantial effect on nutation angle banding artifacts, but do not affect relaxation-dependent artifacts nearly as much.

There is a threshold for field inhomogeneity beyond which low ω_1 imaging becomes unacceptable. Relaxation-dependent artifacts are worse for larger spin lock durations and higher B_0 field inhomogeneities and so the threshold is quantified in terms of τ and ΔB_0 . As stated previously, $T2\rho$ relaxation will change the angle between the effective field and the initially excited magnetization, so artifacts are significant for when times $\tau \sim T2\rho$ and the difference angle between the initial excitation and the effective field

$$\Delta\psi = \alpha - \phi \tag{37}$$

is appreciable. There are three regimes for relaxation-dependent artifacts. For large $\Delta\psi$, there is a significant amount of $T2\rho$ relaxation at long τ durations. $T2\rho$ relaxation can be easily quantified because a large component of the magnetization is perpendicular to the effective field. Conversely, for small $\Delta\psi$, $T1\rho$ relaxation can be easily

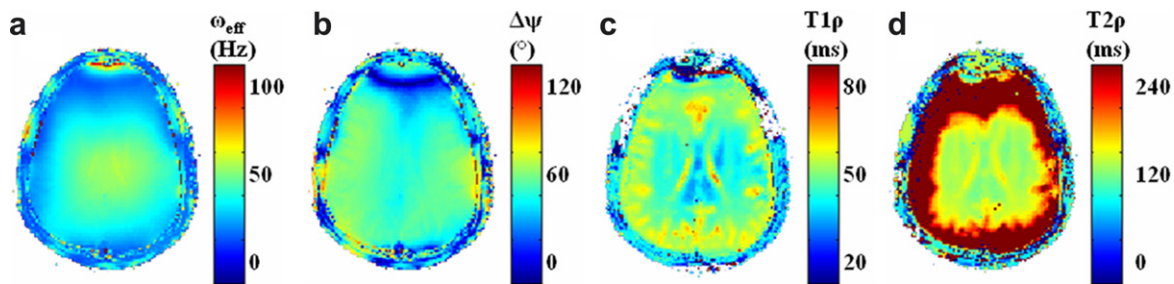


Fig. 8. The origin of relaxation-dependent artifacts in Fig. 6 and 7 is detailed. (a) The effective field ($\omega_{\text{eff}} = \sqrt{\omega_1 + \Delta\omega_0}$) varies spatially at $\omega_1 = 25$ Hz primarily because of variations in ΔB_0 at 3 T. (b) The angular difference between initial excitation and the orientation of the effective field ($\Delta\psi = \alpha - \varphi$). (c and d) $T1\rho$ and $T2\rho$ relaxation maps obtained from Eq. (9) using the transient solutions to the Bloch equations.

quantified, because a large component of the magnetization is parallel to the effective field. Only gradients in $\Delta\psi$ will cause artifacts, because of significant differences in the relaxation times $T1\rho$ and $T2\rho$. In the third regime, when $\Delta\psi \sim 45^\circ$, $T1\rho$ and $T2\rho$ can be quantified, but a convergent solution is less likely. Fig. 8 demonstrates how $\Delta\psi$ affects quantification of $T1\rho$ and $T2\rho$. While both $T1\rho$ and $T2\rho$ depend on ω_{eff} (Fig. 8a), there is a clear spatial dependence of the relaxation times on $\Delta\psi$ (Fig. 8b). For example, where $\Delta\psi$ is large, $T2\rho$ takes on usual brain tissue values ($T2\rho = 140$ ms, Fig. 8d), but when $\Delta\psi$ is small, the magnetization lies parallel to the effective field and $T2\rho$ quantification is not possible. Conversely, $T1\rho$ is quantified when $\Delta\psi$ is small (Fig. 8c), but more difficult when $\Delta\psi$ is large, such as in the frontal cortex. $T1\rho$ is nearly 5 ms lower in the midbrain white matter regions ($\Delta\psi = 45^\circ$) than in the white matter regions of the periphery ($\Delta\psi < 45^\circ$).

5. Discussion

Section 2.5 and Fig. 4 suggest that the ΔB_0 and B_1 insensitive pulse sequence is the most robust against variations in B_0 and B_1 field gradients. Furthermore, the insensitivity of the sequence may be further improved by decomposing the central $\mathbf{R}_y(180^\circ)$ into a composite 180° pulse or substitution with an adiabatic refocusing pulse.

While the foregoing theory entirely corrects for nutations about the effective magnetic field, magnetization dynamics are complicated by relaxation processes. Tissue relaxation during a cw pulse is a complex process that depends on ω_1 , $\Delta\omega_0$ and the component of magnetization parallel ($T1\rho$) or perpendicular ($T2\rho$) to the applied RF field. In general, the system is driven by ω_1 and damped by both $T1$ and $T2$ relaxation until it approaches a steady-state magnetization parallel to the effective field [28]. True monoexponential $T1\rho$ relaxation is observed by flipping the magnetization parallel to ω_1 on-resonance and is distorted by $\Delta\omega_0$ and $T2\rho$. When $\omega_1 \ll \Delta\omega_0$, $\alpha = 90^\circ$ or both, these effects compound to cause the magnetization to deviate from monoexponential $T1\rho$ relaxation and cause additional image artifacts.

$T1\rho$ relaxation measurements are a useful diagnostic tool in clinical imaging and any off-resonance spins interfere with $T1\rho$ quantification. In particular, a $T1\rho$ map dis-

plays the spatial variation in $T1\rho$ across the sample. Often the $T1\rho$ map contains artifacts, even if a single $T1\rho$ -weighted image is artifact free, because the decay of spin magnetization is no longer monoexponential. The $T1\rho$ map is improved by the ΔB_0 and B_1 insensitive pulse sequence and the possibility is now available for tissue studies of very low frequency $T1\rho$ dispersion. Several $T1\rho$ -weighted images collected at low frequency ω_1 may be more sensitive to residual dipolar interactions ($\omega_D \sim 200$ Hz) in tissues and provide a useful form of dipolar contrast among tissues composed of oriented collagen, muscle fibers or myelinated axons. As in Fig. 8, combined quantification of $T1\rho$ and $T2\rho$ is also possible, but must be interpreted in the context of a spatially varying effective field and usually both relaxation times will not be quantifiable simultaneously in a pixel.

Very low amplitude spin locking offers several interesting imaging capabilities. As Santyr, et al. initially suggested, it is possible to estimate the contribution of the local static field B_{loc} by measuring $T1\rho$ dispersion in tissues [30]. In practice, at spin lock amplitudes $\omega_1 \sim \gamma B_{\text{loc}}$ the contribution of the local static fields confounds a measurement of $T1\rho$ because they induce oscillations of the magnetization about an effective field in the case of either off-resonance spins, chemical shift and secular J -coupling. And while this manuscript makes use of the Bloch equations, it can be shown using product operator theory that *any* static interaction that commutes with the spin operator I_z will be refocused. In this way, a low amplitude spin lock dispersion measurement can be used to probe dynamical interactions or spin diffusion independent of spin nutation about the effective field.

Low frequency $T1\rho$ -weighted imaging has two potential applications in medicine where $\omega_1 \sim \gamma B_{\text{loc}}$. We suspect that it will generate useful contrast in indirectly detected H_2^{17}O for studies of brain metabolism because of the low-frequency scalar coupling between ^1H and ^{17}O [13]. A bolus of enriched $^{17}\text{O}_2$ may be given to a human subject and converted to metabolically produced H_2O^{17} . The magnetically active ^{17}O nucleus interacts with water protons through scalar coupling and differences between low frequency ($\omega_1 \sim J_{\text{H-O}}$) and high frequency ($\omega_1 \gg J_{\text{H-O}}$) $T1\rho$ -weighted images are sensitive to ^{17}O . This phenomenon has been observed in rat models, but is limited by B_0 field inhomoge-

neities in the low frequency regime ($\omega_1 \sim J_{H-O}$) [16]. In addition, static dipole–dipole interactions are known to exist in oriented tissues such as collagen layers of human cartilage [5,31]. In the anisotropic environment of collagen tissues, 1H – 1H static dipole–dipole interactions are partially averaged, such that $\omega_D \sim 200$ Hz. Low frequency $T1\rho$ -weighted imaging may be sensitive to changes in this interaction, especially during diseases of the cartilage like osteoarthritis.

6. Conclusion

The origin of inhomogeneous $\Delta\omega_0$ and ω_1 field artifacts in $T1\rho$ -weighted images are oscillations about the effective field at low ω_1 and imperfect flip angles $\alpha = 90^\circ$ at all field strengths. We introduced a spin locking pulse sequence that almost entirely compensates for both types of artifacts at all field strengths. The sequence combines the familiar spin echo with a final pulse phase inversion to flip magnetization along the $-z$ -axis. Consequently, several experimental images were shown on agarose gel and water fat phantoms confirming both $\Delta\omega_0$ and ω_1 insensitivity. These results were confirmed with the derived theory and simulation. The foregoing theory and sequence should be useful for spin locking in the low frequency ($\omega_1 = 0$ –600 Hz) regime and generate useful contrast for $T1\rho$ -weighted imaging applications.

References

- [1] A.G. Redfield, Nuclear magnetic resonance saturation and rotary saturation in solids, *Phys. Rev.* 98 (1955) 1787–1809.
- [2] U. Duvvuri, A.D. Goldberg, J.K. Kranz, L. Hoang, R. Reddy, F.W. Wehrli, A.J. Wand, S.W. Englander, J.S. Leigh, Water magnetic relaxation dispersion in biological systems: the contribution of proton exchange and implications for the noninvasive detection of cartilage degradation, *Proc. Natl. Acad. Sci. USA* 98 (2001) 12479–12484.
- [3] H.I. Makela, O.H.J. Grohn, M.I. Kettunen, R.A. Kauppinen, Proton exchange as a relaxation mechanism for T-1 in the rotating frame in native and immobilized protein solutions, *Biochem. Biophys. Res. Commun.* 289 (2001) 813–818.
- [4] R.R. Knispel, R.T. Thompson, M.M. Pintar, Dispersion of proton spin–lattice relaxation in tissues, *J. Magn. Reson.* 14 (1974) 44–51.
- [5] S.V. Akella, R.R. Regatte, A.J. Wheaton, A. Borthakur, R. Reddy, Reduction of residual dipolar interaction in cartilage by spin-lock technique, *Magn. Reson. Med.* 52 (2004) 1103–1109.
- [6] O.H.J. Grohn, J.A. Lukkarinen, M.J. Silvennoinen, A. Pitkanen, P.C.M. van Zijl, R.A. Kauppinen, Quantitative magnetic resonance imaging assessment of cerebral ischemia in rat using on-resonance T-1 in the rotating frame, *Magn. Reson. Med.* 42 (1999) 268–276.
- [7] O.H. Grohn, H.I. Makela, J.A. Lukkarinen, L. DelaBarre, J. Lin, M. Garwood, R.A. Kauppinen, On- and off-resonance $T1\rho$ MRI in acute cerebral ischemia of the rat, *Magn. Reson. Med.* 49 (2003) 172–176.
- [8] O.H.J. Grohn, M.I. Kettunen, H.I. Makela, M. Penttonen, A. Pitkanen, J.A. Lukkarinen, R.A. Kauppinen, Early detection of irreversible cerebral ischemia in the rat using dispersion of the magnetic resonance imaging relaxation time, $T1\rho$, *J. Cereb. Blood. Flow. Metab.* 20 (2000) 1457–1466.
- [9] H.J. Aronen, U.A. Ramadan, T.K. Peltonen, A.T. Markkola, J.I. Tantt, J. Jaaskelainen, A.M. Hakkinen, R. Sepponen, 3D spin-lock imaging of human gliomas, *Magn. Reson. Imaging* 17 (1999) 1001–1010.
- [10] G.E. Santyr, R.M. Henkelman, M.J. Bronskill, Spin locking for magnetic-resonance imaging with application to human-breast, *Magn. Reson. Med.* 12 (1989) 25–37.
- [11] R.R. Regatte, S.V.S. Akella, A.J. Wheaton, G. Lech, A. Borthakur, J.B. Kneeland, R. Reddy, 3D-T-1 rho-relaxation mapping of articular cartilage: in vivo assessment of early degenerative changes in symptomatic osteoarthritic subjects, *Acad. Radiol.* 11 (2004) 741–749.
- [12] J.D. Auerbach, W. Johannessen, A. Borthakur, A.J. Wheaton, C.A. Dolinskas, R.A. Balderston, R. Reddy, D.M. Elliott, In vivo quantification of human lumbar disc degeneration using T-1 rho-weighted magnetic resonance imaging, *Eur. Spine J.* 15 (2006) S338–S344.
- [13] R. Reddy, A.H. Stolpen, J.S. Leigh, Detection of O-17 by proton T-1P dispersion imaging, *J. Magn. Reson. B* 108 (1995) 276–279.
- [14] D.R. Taylor, H. Poptani, J.D. Glickson, J.S. Leigh, R. Reddy, High-resolution assessment of blood flow in murine RIF-1 tumors by monitoring uptake of H217O with proton $T1\rho$ -weighted imaging, *Magn. Reson. Med.* 49 (2003) 1–6.
- [15] D.R. Taylor, A. Roy, R.R. Regatte, S.V.S. Akella, J.S. Leigh, R. Reddy, Measuring regional blood flow in the rat brain using indirect 17O magnetic resonance imaging, *Proc. Intl. Soc. Magn. Reson. Med. ISMRM-ESMRB Joint Annual Meeting, Glasgow, 2001*, p. 356.
- [16] D.R. Taylor, A. Roy, R.R. Regatte, S.R. Charagundla, A.C. McLaughlin, J.S. Leigh, R. Reddy, Indirect 17O-magnetic resonance imaging of cerebral blood flow in the rat, *Magn. Reson. Med.* 49 (2003) 479–487.
- [17] S.R. Charagundla, A. Borthakur, J.S. Leigh, R. Reddy, Artifacts in T-1 rho-weighted imaging: correction with a self-compensating spin-locking pulse, *J. Magn. Reson.* 162 (2003) 113–121.
- [18] A. Borthakur, A. Wheaton, S.R. Charagundla, E.M. Shapiro, R.R. Regatte, S.V.S. Akella, J.B. Kneeland, R. Reddy, Three-dimensional $T1\rho$ MRI at 1.5 Tesla, *J. Magn. Reson. Imaging* 17 (2003) 730–736.
- [19] M. Garwood, L. DelaBarre, The return of the frequency sweep: designing adiabatic pulses for contemporary NMR, *J. Magn. Reson.* 153 (2001) 155–177.
- [20] A.J. Wheaton, A. Borthakur, M. Corbo, S.R. Charagundla, R. Reddy, Method for reduced SAR $T1\rho$ -weighted MRI, *Magn. Reson. Med.* 51 (2004) 1096–1102.
- [21] G.E. Santyr, E.J. Fairbanks, F. Kelcz, J.A. Sorenson, Off-resonance spin locking for MR imaging, *Magn. Reson. Med.* 32 (1994) 43–51.
- [22] E.J. Fairbanks, G.E. Santyr, J.A. Sorenson, One-shot measurement of spin–lattice relaxation-times in the off-resonance rotating-frame using mr-imaging, with application to breast, *J. Magn. Reson. B* 106 (1995) 279–283.
- [23] H.I. Grohn, S. Michaeli, M. Garwood, R.A. Kauppinen, O.H.J. Grohn, Quantitative T-1p and adiabatic Carr-Purcell T-2 magnetic resonance imaging of human occipital lobe at 4 T, *Magn. Reson. Med.* 54 (2005) 14–19.
- [24] I. Solomon, Rotary Spin Echoes, *Phys. Rev. Lett.* 2 (1959) 301–302.
- [25] M. Avison, D. Gochberg, C. Gatenby, J. Gore, H. Zeng, Y. Zhao, A composite spin-lock pulse for $\Delta B_0 + B_1$ insensitive $T1\rho$ measurement, *Proc. Soc. Magn. Reson. Med., ISMRM Annual Meeting, Seattle, Washington, 2006*.
- [26] M.H. Levitt, R. Freeman, Nmr population-inversion using a composite pulse, *J. Magn. Reson.* 33 (1979) 473–476.
- [27] D.W. Marquardt, An algorithm for least-squares estimation of nonlinear parameters, *J. Soc. Ind. Appl. Math.* 11 (1963) 431–441.
- [28] H.C. Torrey, Transient nutations in nuclear magnetic resonance, *Phys. Rev.* 76 (1949) 1059–1068.
- [29] C.M. Collins, S.Z. Li, M.B. Smith, SAR and B-1 field distributions in a heterogeneous human head model within a birdcage coil, *Magn. Reson. Med.* 40 (1998) 847–856.
- [30] G.E. Santyr, R.M. Henkelman, M.J. Bronskill, Variation in measured transverse relaxation in tissue resulting from spin locking with the cpmg sequence, *J. Magn. Reson.* 79 (1988) 28–44.
- [31] Y. Xia, Relaxation anisotropy in cartilage by NMR microscopy (μ MRI) at 14- μ m resolution, *Magn. Reson. Med.* 39 (1998) 941–949.